

---

1 **Comparison of the imaginary partparts of the atmospheric**  
2 **refractive index structure parameter and aerosol flux based**  
3 **on different measurement methods**

4 Renmin Yuan<sup>a</sup> Hongsheng Zhang<sup>b</sup> Jijia Hua<sup>c</sup> Hao Liu<sup>d</sup> Peizhe Wu<sup>a</sup> Xingyu Zhu<sup>a</sup> Jianning Sun<sup>e</sup>

5  
6 <sup>a</sup>School of Earth and Space Science, University of Science and Technology of China, Hefei 230026, PR China

7 <sup>b</sup>Laboratory for Climate and Ocean-Atmosphere Studies, Department of Atmospheric and Oceanic Sciences, School  
8 of Physics, Peking University, Beijing 100081, PR China

9 <sup>c</sup>China Meteorological Administration Xiong'an Atmospheric Boundary Layer Key Laboratory, Xiong'an New Area  
10 071800, PR China

11 <sup>d</sup>School of Mathematics and Physics Anhui Jianzhu University, Hefei 230601, PR China

12 <sup>e</sup>School of Atmospheric Sciences, Nanjing University, Jiangsu, 210093, PR China

13 Correspondence: Yuan Renmin (rmyuan@ustc.edu.cn)

14 Abstract: The complexity of aerosol particle properties and the diversity of characterizations make  
15 aerosol vertical transport flux measurements and analysis difficult. Although there are different  
16 methods, such as aerosol particle number concentration flux and aerosol mass flux based on the eddy  
17 covariance principle, and aerosol mass flux measurements based on the light-propagated large-  
18 aperture scintillation principle, there is a lack of mutual validation among the different methods. In  
19 this paper, a comparison of aerosol mass flux measurements based on the eddy covariance principle  
20 and aerosol mass flux measurements based on the light-propagated large aperture scintillation  
21 principle is carried out. The key idea of aerosol mass flux measurements based on the light-  
22 propagated large-aperture scintillation principle is the determination of the imaginary part of the  
23 atmospheric equivalent refractive index structure parameter (AERISP). In this paper, we ~~will~~ first  
24 compare the AERISPs measured by two different methods and then compare the aerosol mass  
25 vertical transport fluxes obtained by different methods. The experiments were conducted on the  
26 campus of the University of Science and Technology of China (USTC). ~~The~~A light propagation  
27 experiment was carried out between two tall buildings to obtain the imaginary and real parts of ~~the~~  
28 AERISPs for the whole path, which in turn can be used to obtain the aerosol vertical transport flux.  
29 An updated visibility meter is installed on the meteorological tower in the middle of the light path,  
30 which is utilized to obtain the single-point visibility, which is then converted to the imaginary part  
31 of the atmospheric equivalent refractive index (AERI). The imaginary parts of the AERISP were  
32 obtained ~~using~~via spectral analysis with visibility data. The results show that the imaginary parts of  
33 the AERISPs obtained by different methods are in good agreement. The imaginary part of the AERI  
34 measured by the visibility meter and the vertical wind speed obtained by the ultrasonic anemometer  
35 were used for covariance ~~calculation~~calculations to obtain the aerosol vertical transport flux. The  
36 trends ~~of~~in aerosol vertical transport fluxes obtained by ~~the~~ different methods are consistent, and  
37 there are differences in some details, which may be caused by the inhomogeneity of the vertical  
38 transport of aerosol fluxes. The experimental results also ~~show~~showed that urban green land is a sink  
39 area for aerosol particles.

40 Keywords: light propagation, scintillation, atmospheric equivalent refractive index, structure  
41 parameter, eddy covariance, aerosol fluxes

带格式的: 字体: Times New Roman

---

# 1 Introduction

42  
43 Atmospheric aerosols are solid or liquid particles suspended in the atmosphere that can affect  
44 public health, reduce near-surface visibility, decrease direct radiation from the air, and act as  
45 condensation nuclei affecting cloud structure and distribution (McNeill, 2017; Rosenfeld et al., 2014).  
46 Human activities have dramatically altered air quality, climate and the Earth system. The expansion  
47 of urban, agricultural and industrial areas and changes in the nature of land use have increased  
48 aerosol concentrations. Due to the complexity of aerosols, many observations have been carried out  
49 from different perspectives. However, most of the current observations only measure the state  
50 characteristics of aerosols, such as concentration, particle size distribution, and composition, and  
51 what is obtained is an average characterization of aerosol properties (Krieger et al., 2012).

52 Aerosol particles in the atmosphere will follow atmospheric motion, which is manifested in  
53 the uneven distribution of aerosol particle concentrations in space and time. On the  
54 one hand, the unevenly distributed aerosol particles will have a corresponding effect on the light  
55 wave propagating in the atmosphere, and on the other hand, we can understand the  
56 distribution characteristics of aerosol particles based on the optical effect of aerosol particles and  
57 then obtain more information about the transportation of aerosols.

58 Previously, Yuan et al. (2015, 2016) introduced the concepts of the atmospheric equivalent  
59 refractive index (AERI) and the atmospheric equivalent refractive index structure parameter  
60 (AERISP). The term AERISP corresponds to the equivalent medium containing air and aerosol  
61 particles, relative to the commonly used atmospheric refractive index structure parameter (RISP)  
62 obtained from single-point measurements (Wyngaard et al., 1971). The AERI includes real and  
63 imaginary parts, and accordingly, the AERISP also includes real and imaginary parts of the structure  
64 parameters. When the working wavelength is in the atmospheric transparent band, the light wave is  
65 almost not absorbed by the gas components in the atmosphere, and the attenuation of the light wave  
66 is caused mainly by the extinction of aerosol particles. Theoretical analysis shows that  
67 the imaginary part of the AERISP is determined by the fluctuation of aerosol concentration.  
68 The real part of the AERISP corresponds to the atmospheric temperature variation.  
69 Furthermore, it is assumed (Yuan et al., 2021). Experiments have shown that the aerosol  
70 concentration variations follow the same pattern as the scalar motion, which is in line with  
71 the similar theory of the surface layer, and thus, the vertical transport flux of aerosol particles locally  
72 homogeneous isotropic turbulence as air molecules (Martensson et al., 2006; Vogt et al., 2011a; Ren  
73 et al., 2020); that is, the fluctuation in the near-surface layer particle concentration follows the '-5/3'  
74 power law under unstable atmospheric stratification, and the concentration-velocity cospectra for  
75 particle number flux follow the '-4/3' power law, similar to the temperature-velocity cospectra

---

76 (Kaimal et al., 1972). Therefore, the distribution of small particles can be obtained by using the  
77 imaginary part of the AERISP (Yuan et al., 2016; Yuan et al., 2019). AERISP observations are carried  
78 out in many places, and then the aerosol flux is obtained by combining the similarity theory, regarded  
79 ~~However, there is a lack of experimental verification of the imaginary structure parameter and~~  
80 ~~aerosol flux observations.~~ Currently, the imaginary part of the AERISPs is only obtained using large-  
81 aperture scintillometer (LAS) measurements, so it is necessary to carry out measurements of the  
82 imaginary part of the AERISPs based on other different methods, as well as measurements of aerosol  
83 fluxes based on different methods a passive conservative quantity, similar to the temperature field.

84 The reference to the measurement of the imaginary part of the AERISP and the aerosol vertical  
85 transport flux using the light propagation principle is naturally associated with the current  
86 widespread use of LASs based on the light propagation principle for the measurement of the sensible  
87 heat flux in the surface layer (Moene et al., 2009). Comparative validation of this measurement is  
88 obtained using eddy covariance (EC) techniques (Zhang and Zhang, 2015). EC measurements require  
89 a fast response of the sensing elements for wind speed and air temperature. Similar to the validation  
90 of LAS measurements of sensible heat fluxes, EC measurements were also considered for aerosol  
91 vertical transport flux validation. Measurements of aerosol particle number concentration fluxes  
92 using eddy covariance methods have been implemented at many locations. Then, it can be assumed  
93 that the aerosol mass concentration fluctuation also follows the locally homogeneous isotropic  
94 turbulence theory; thus the aerosol mass concentration structure parameter can be defined (Yuan et  
95 al., 2016). Based on the fact that the temperature structure function satisfies the surface layer  
96 similarity theory and thus the surface layer sensible heat flux is obtained from the temperature  
97 structure parameter (Wyngaard et al., 1971), it is analogous to that, based on the fact that the aerosol  
98 mass concentration structure parameter satisfies the surface similarity theory, the surface layer  
99 aerosol mass flux is obtained from the aerosol mass concentration structure parameter (Gordon  
100 et al., 2011; Voegt 2016; Yuan et al., 2011; Ripamonti et al., 2013 2019). Using the relationship between  
101 the temperature-real part of the AERI and aerosol mass concentration-imaginary part of the AERI,  
102 the temperature structure parameter and aerosol mass concentration structure parameter are obtained  
103 from the real part of the AERISP and imaginary part of the AERISP.

104 From this, the aerosol mass concentration flux can be obtained, utilizing large aperture  
105 scintillometer (LAS) measurements. AERISP observations are carried out in many places, after  
106 which the aerosol flux is obtained via the similarity theory (Yuan et al., 2016; Yuan et al., 2019).  
107 ~~However, there is a lack of experimental verification of the imaginary structure parameter and~~  
108 ~~aerosol flux observations.~~ ~~We attempted to measure the~~ Currently, the imaginary part of the AERISPs  
109 is obtained using only LAS measurements; therefore, it is necessary to carry out measurements of

the imaginary part of the AERISPs based on other methods, as well as measurements of aerosol fluxes based on different methods.

At present, in addition to the previously mentioned measurements of the AERISP based on the principle of long-range light propagation and the similarity theory of the surface layer to obtain the vertical transport flux of aerosol mass in the surface layer, several studies utilize eddy covariance (EC) techniques with fluctuations in aerosol particle number concentration flux and fluctuation in vertical wind speed to obtain the flux of the number concentration of aerosol particles. Such measurements are carried out in many places (Gordon et al., 2011; Vogt et al., 2011b; Ripamonti et al., 2013). Measurements have revealed quantitative relationships for urban aerosol fluxes among urban vehicle emissions and meteorological conditions (Jarvi et al., 2009), and characteristics of sea salt transport, and aerosol properties (Nemitz et al., 2009). We followed this approach and conducted several measurements in 2019 and 2020 to measure aerosol particle number concentration fluxes using an eddy covariance-correlation system consisting of combining a fast-response particle counter with an ultrasonic anemometer, which has with a response frequency of up to 10 Hz, and to calculate aerosol mass concentration fluxes by simultaneously measured parameters such as measuring aerosol particle size distribution, mass concentration concentrations, forward scattering coefficient, and coefficients, extinction coefficient to calculate the aerosol mass concentration flux coefficients, and other parameters. For half of the experimental period, the trends of the measurements with of the two methods was were the same, while the other periods differed greatly (more unpublished experimental results unpublished). The main reason may be the very weak extinction of aerosol particles with that scales much smaller than the working wavelength. Second, the aerosol number concentration flux must be combined with parameters such as particle size distribution, complex refractive index of aerosol particles and aerosol particle density, which also need to be sampled in real time. This also illustrates the complexity of aerosol particles.

According to the definition of the imaginary part of the AERISP, the validation work can be realized by choosing an instrument for rapid measurement of the atmospheric extinction coefficient and an ultrasonic anemometer to form an EC system. However, the direct and rapid measurement of the atmospheric extinction coefficient is difficult to realize. The imaginary part of the AERI is proportional to the atmospheric extinction coefficient and inversely proportional to the atmospheric visibility, so it is possible to analyze the results of the visibility meter to obtain the imaginary part of the AERISP at a certain point. However, the conventional visibility meter has a slow response and low sampling frequency, which is not suitable for correlating with the vertical velocity to obtain the aerosol flux, and Ren et al. (2020) improved the conventional visibility meter by obtaining visibility data at 1 Hz and then using the eddy covariance method to obtain the vertical aerosol transport flux based on the relationship between visibility and aerosol mass concentration (Ren et al., 2020).

带格式的: 字体颜色: 黑色

Inspired by their work, we use the Recently, Ren et al. (2020) improved upon the conventional visibility meter method to obtain 1 Hz visibility data, and subsequently utilized the EC method to obtain the aerosol vertical transport flux based on the relationship between visibility and aerosol mass concentration. The visibility is approximately inversely proportional to the atmospheric extinction coefficient, i.e., approximately inversely proportional to the imaginary part of the AERI; therefore their theory of obtaining the aerosol vertical transport flux by the EC method is close to theory of the aerosol vertical transport flux based on the measurement of the long-path light propagation. Inspired by their work, we used an improved visibility meter in this study to obtain visibility data at a higher frequency of 1 Hz and ~~correlate~~cross-correlated the data with ultrasonic anemometer measurements to potentially utilize the obtained aerosol vertical transport fluxes to achieve experimental validation of the imaginary part of the AERISP and aerosol flux observations.

The theoretical and experimental introduction is given in the second part of the paper, the experimental results are given in the third part, and the conclusions and discussion are given in the fourth part.

## 2 Theoretical methods and experiments

The AERISP and ~~the~~ aerosol vertical transport flux are the topics of interest in this paper. In this section, definitions and theoretical expressions for these parameters are given, as well as how the measurements were carried out.

### 2.1 The imaginary part of the AERISP

~~Normally, the atmosphere consists of gas molecules and aerosol particles. When thea light beam is transmittedpropagates in the atmosphere, due to the inhomogeneous distribution of the atmospheric gas refractive index, the beam will be refracted and diffracted, which results in addition to the unevenlyan inhomogeneous spatial distribution of the beam energy due to the refraction diffraction phenomenon caused by the fluctuation of the refractive index caused by. Due to the existence of aerosol particles in the fluctuation of temperatureatmosphere, the beam will be scattered and absorbed, and the energy is also attenuated by the absorption and scattering of aerosol particles. of the beam will be weakened.~~ Therefore, the ~~atmosphere~~atmospheric gas molecules and aerosol particles can be taken as a whole, called the equivalent medium; thus, the ~~atmospheric~~ atmospheric equivalent refractive index (AERI)  $n_{equ}$  concept is introduced (van de Hulst, 1957; Yuan et al., 2021),

$$n_{equ} = n_m + i \frac{2\pi}{\eta^3} \int_0^\infty S(0) \frac{dN}{dD} dD \quad n_{equ} = n_m + i \frac{2\pi}{\eta^3} \int_0^\infty S(0) \frac{dN}{dD} dD \quad (1)$$

176 where  $n_m$  is the refractive index of atmospheric molecules,  $\eta$  is the wavenumber of light waves, and  
 177  $i$  denotes an imaginary number.  $S(0)$  is the forward scattering function (0 in parentheses is the  
 178 scattering angle).  $N$  is the number of aerosol particles per unit volume, and  $dN/dD$  is the size  
 179 distribution of aerosol [partiele-sizesparticles](#).

180 The [equivalent refractive indexAERI](#) consists of real and imaginary parts denoted by  $n_{Re}$  and  
 181  $n_{Im}$ , respectively; i.e.,  $n_{eff1equ} = n_{Re} + in_{Im}$ . The real part is the refractive index of the molecule, and  
 182 the imaginary part is.

183 
$$n_{Im} = \frac{2\pi}{\eta^3} \int_0^{\infty} \text{Re}[S(0)] \frac{dN}{dD} dD \quad n_{Im} = \frac{2\pi}{\eta^3} \int_0^{\infty} \text{Re}[S(0)] \frac{dN}{dD} dD$$
  
 184 (2)

185 ~~It is known that the~~The atmospheric extinction coefficient has a similar form(Liou, 2002):

186 
$$\beta_{ext} = \frac{4\pi}{\eta^2} \int_0^{\infty} \text{Re}[S(0)] \frac{dN}{dD} dD \quad \beta_{ext} = \frac{4\pi}{\eta^2} \int_0^{\infty} \text{Re}[S(0)] \frac{dN}{dD} dD$$
  
 187 (3)

188 From Eqs (2) and (3), we can see that

189 
$$n_{Im} = \lambda \beta_{ext} / 4\pi$$
  
 190 (4)

190 where  $\lambda$  is the working wavelength ( $\lambda=2\pi/\eta$ ). ~~Based on the relationship between the aerosol extinction~~  
 191 ~~coefficient and visibility ( $V=3.912/\beta_{ext}$ ), the aerosol extinction coefficient can be deduced from~~  
 192 ~~visibility measurements, and then the imaginary part of the AERI can be obtained based on Eq.~~

193 ~~Due to the dependence of the reduction in contrast on atmospheric absorption and scattering,~~  
 194 ~~the following relationship between visibility  $V$  and extinction coefficient  $\beta_{ext}$  can be obtained:~~  
 195  ~~$V=3.912/\beta_{ext}$  (Middleton, 1957;Charlson, 1969). Thus,  $\beta_{ext}$  in the relationship ( $V=3.912/\beta_{ext}$ )~~  
 196 ~~represents the extinction by all compositions in the air, e.g., absorption and scattering of aerosols~~  
 197 ~~and atmospheric molecular extinction. In other words, the visibility-based extinction coefficient is~~  
 198 ~~sum of the extinction coefficient from aerosol absorption and scattering and the atmospheric~~  
 199 ~~molecular extinction coefficient. However, in the urban atmosphere, the extinction effect of aerosols~~  
 200 ~~is much greater than that of atmospheric molecules. Therefore, the contribution of extinction by~~  
 201 ~~atmospheric molecules can be neglected. Therefore, the aerosol extinction coefficient can be~~  
 202 ~~deduced from visibility measurements, and the imaginary part of the AERI can be obtained based~~  
 203 ~~on Eq. (4).~~

204 Experiments show that the temperature fluctuation satisfies the turbulence "2/3" law(Liu et al.,  
 205 2017), and ~~according due to the relationship between small relative changes in pressure and air~~  
 206 ~~temperature and (unit K) occurring over a short period, the change in the real part of the AERI, has~~  
 207 ~~a good linear relationship with the temperature change, and the fluctuation of in the real part of the~~  
 208 ~~AERI also satisfies the turbulence "2/3" law; thus, we can define the structure parameter of~~  
 209 ~~temperature,  $C_T^2$ , and the real part of the AERISP  $C_{n,Re}^2$ . Therefore, general scalars can be extended,~~  
 210 ~~such as the fluctuation of the imaginary part of the AERISP and the fluctuation of the atmospheric~~  
 211 ~~extinction coefficient. Thus, we can assume that the imaginary part of the AERI satisfies the~~  
 212 ~~turbulence "2/3" law; that is, the structure function of the imaginary part of the AERI  $D_{n,Im}(r)$  ( $r$  is~~  
 213 ~~the separation) can be defined as~~

带格式的: 缩进: 左侧: 0.02 厘米, 首行缩进: 2.7 字符, 段落间距段前: 0 磅, 段后: 3.9 磅, 行距: 多倍行距 1.23 字符

带格式的: 字体颜色: 黑色

带格式的: 字体颜色: 黑色

带格式的: 字体颜色: 黑色

$$D_{n,lm}(r) = \overline{[n_{lm}(\vec{x}) - n_{lm}(\vec{x} + \vec{r})]^2} = C_{n,lm}^2 r^{2/3} D_{n,lm}(r) = \overline{[n_{lm}(\vec{x}) - n_{lm}(\vec{r} + \vec{x})]^2} = C_{n,lm}^2 r^{2/3} \quad (5)$$

where  $\vec{x}, \vec{r} + \vec{x}$  are the coordinates of two points in space,  $\vec{r}$  is the separation vector,  $C_{n,lm}^2$  is the imaginary part of the AERISP, and the overbar indicates the mean.

Thus, we can introduce the imaginary part of the AERISP  $C_{n,lm}^2$ , a parameter used to describe the fluctuation intensity of the imaginary part of the AERI.  $C_{n,lm}^2$  should be the structure parameter for the imaginary part of the AERI, conveniently denoted as the imaginary part of the AERISP. Correspondingly, we can introduce the structure parameter of the atmospheric extinction coefficient  $C_{\beta_{ext}}^2$  and the structure parameter of the fluctuation of the aerosol mass concentration  $C_M^2$ .

## 2.2 Two methods of equivalent refractive index structure parameter AERI measurement

From the definition of the AERISP in the last part and the relationship between the AERI and the extinction coefficient, it can be seen that the AERISP has an important influence on light propagation in the atmosphere, and thus, the AERISP can be estimated from the light intensity fluctuations in light propagation intensity and the monitoring of the extinction coefficient. This section describes how to measure the AERISP with the help of via two methods.

### 2.2.1 Long-Path Light Propagation Methods

When an approximately collimated light beam in the transparent band of the atmosphere is selected and propagated over a distance, the light intensity at the receiving end fluctuates. The fluctuation in light intensity has two causes: one is the uneven distribution of the real part of the AERI caused by the temperature fluctuation, and the other is the uneven distribution of the imaginary part of the AERI caused by the uneven distribution of aerosol particles. Assuming that the above two causes are not related, they can be decomposed. Theoretical analysis shows that the power spectral density expression for is usually used to characterize the fluctuation in light intensity. Through spectral analysis, the power spectral density of light intensity fluctuations can be decomposed into the contribution of the imaginary part of the AERISP and the contribution of the real part of the AERISP. The contribution of the inhomogeneous distribution of the imaginary part of the AERI to the fluctuation of the light intensity fluctuation is expressed as the temporal spectrum  $W_{ln,lm}(f)$ . (Yuan et al., 2015).

$$W_{ln,lm}(f) = 64\pi^2 \eta^2 \int_0^L dx \int_{2\pi f/v}^{\infty} \Phi_{n,lm}(\kappa) \cos^2 \left[ \frac{\kappa^2 x(L-x)}{2\eta L} \right] \left[ (\kappa v)^2 - (2\pi f)^2 \right]^{-1/2} \cdot \left[ \frac{2J_1\left(\frac{D_r \kappa x}{2L}\right)}{D_r \kappa x / 2L} \right]^2 \left[ \frac{2J_1\left(\frac{D_r \kappa(L-x)}{2L}\right)}{D_r \kappa(L-x) / 2L} \right]^2 \kappa d\kappa$$

$$W_{\ln I, \text{Im}}(f) = 64\pi^2 \eta^2 \int_0^L dx \int_{2\pi f/v}^{\infty} \Phi_{n, \text{Im}}(\kappa) \cos^2 \left[ \frac{\kappa^2 x(L-x)}{2\eta L} \right] [(\kappa v)^2 - (2\pi f)^2]^{-1/2} \cdot$$

$$\frac{2J_1\left(\frac{D_r \kappa x}{2L}\right)}{D_r \kappa x / 2L} \frac{2J_1\left(\frac{D_t \kappa(L-x)}{2L}\right)}{D_t \kappa(L-x) / 2L} \kappa d\kappa \quad (6)$$

where  $f$  is the frequency of the log-intensity spectrum,  $\eta$  is the wavenumber of the spherical wave ( $\eta=2\pi/\lambda$ ,  $\lambda$  is the light wavelength),  $x$  is the position of the propagating wave,  $L$  is the length of the propagation path,  $\kappa$  is the wavenumber of the two-dimensional log-intensity spectrum, and  $\Phi_{n, \text{Im}}$  is the spectrum of the imaginary parts of the refractive index, where the subscript  $n$  denotes the refractive index and the subscript  $\text{Im}$  denotes the imaginary parts of the refractive index.  $D_t$  is the transmitting aperture diameter,  $D_r$  is the receiving aperture diameter ( $D_t$  and  $D_r$  are usually identical for an LAS),  $v$  is the transverse wind speed and  $J_1$  is the first-order Bessel function. The widely used von Karman spectral form for  $\Phi_{n, \text{Im}}$  is adopted in this study (Andrews and Phillips, 2005), which and can be expressed as follows:

$$\Phi_{n, \text{Im}}(\kappa) = 0.033 C_{n, \text{Im}}^2 \left( \kappa^2 + \frac{1}{L_0^2} \right)^{-\frac{11}{6}} e^{-\frac{\kappa^2 l_0^2}{5.92^2}} \Phi_{n, \text{Im}}(\kappa) = 0.033 C_{n, \text{Im}}^2 \left( \kappa^2 + \frac{1}{L_0^2} \right)^{-\frac{11}{6}} e^{-\frac{\kappa^2 l_0^2}{5.92^2}} \quad (7)$$

Here,  $L_0$  is the outer scale of turbulence, and  $l_0$  is the inner scale of turbulence.

Substituting Eq. (7) into Eq. (6) and integrating the right-hand side of Eq. (6) yields,

$$W_{\ln I, \text{Im}}(f) = 0.129 C_{n, \text{Im}}^2 \eta^2 L v^{5/3} \left[ f^2 + \left( \frac{v}{2\pi L_0} \right)^2 \right]^{-4/3}$$

$$W_{\ln I, \text{Im}}(f) = 0.129 C_{n, \text{Im}}^2 \eta^2 L v^{5/3} \left[ f^2 + \left( \frac{v}{2\pi L_0} \right)^2 \right]^{-4/3} \quad (8)$$

Using Eq. (8), the imaginary part of the AERISP can be determined based on the shape of the spectrum while being constrained by the low-frequency variance of the light intensity fluctuation from the imaginary part of the AERISP.

To carry out a comparative analysis with the results of the real part of the AERISP, the expression for the power spectral density of the logarithmic light intensity fluctuation  $W_{\ln I, \text{Re}}(f)$  due to the real part of the AERI is also given here as (Clifford, 1971; Nieveen et al., 1998),

$$W_{\ln I, \text{Re}}(f) = 64\pi^2 \eta^2 \int_0^L dx \int_{2\pi f/v}^{\infty} \Phi_{n, \text{Re}}(\kappa) \sin^2 \left[ \frac{\kappa^2 x(L-x)}{2\eta L} \right] [(\kappa v)^2 - (2\pi f)^2]^{-1/2} \cdot$$

$$\frac{2J_1\left(\frac{D_r \kappa x}{2L}\right)}{D_r \kappa x / 2L} \frac{2J_1\left(\frac{D_t \kappa(L-x)}{2L}\right)}{D_t \kappa(L-x) / 2L} \kappa d\kappa$$



$$W_{\ln I, \text{Re}}(f) = 64\pi^2\eta^2 \int_0^L dx \int_{2\pi f/v}^{\infty} \Phi_{n, \text{Re}}(\kappa) \sin^2\left[\frac{\kappa^2 x(L-x)}{2\eta L}\right] [(\kappa v)^2 - (2\pi f)^2]^{-1/2} \cdot$$

$$\frac{2J_1\left(\frac{D_r \kappa x}{2L}\right)}{D_r \kappa x / 2L} \frac{2J_1\left(\frac{D_r \kappa(L-x)}{2L}\right)}{D_r \kappa(L-x) / 2L} \kappa d\kappa \quad (9)$$

Integrating Eq. (9) yields the fluctuation variance of the log light intensity as

$$\sigma_{\ln I, \text{Re}}^2 = \int_0^{\infty} W_{\ln I, \text{Re}}(f) df = 0.89 C_{n, \text{Re}}^2 L^3 D_r^{-7/6} D_r^{-7/6}$$

$$\sigma_{\ln I, \text{Re}}^2 = \int_0^{\infty} W_{\ln I, \text{Re}}(f) df = 0.89 C_{n, \text{Re}}^2 L^3 D_r^{-7/6} D_r^{-7/6} \quad (10)$$

The real part of the AERISP is usually calculated using Eq. (10) (Wang et al., 1978).

The calculation steps for the real and imaginary parts of AERISP are as follows: first, power spectrum analysis or correlation analysis of the irradiance fluctuation data are performed; then, the irradiance fluctuation data are decomposed into high-frequency and low-frequency parts; the high-frequency part corresponds to the contribution of the real part of the AERI; and the low-frequency part of the fluctuation corresponds to the contribution of the imaginary part of the AERI; finally, the real part of the AERISP  $C_{n, \text{Re}}^2$  can be obtained from Eq. (10); and the imaginary part of the AERISP  $C_{n, \text{Im}}^2$  can be obtained from the low-frequency part of the irradiance fluctuation.

## 2.2.2 Spectral analysis methods for single-point measurements

Aerosol particles follow atmospheric motion, which is consistent with general atmospheric motion characteristics, and the "-5/3" law can be used to characterize the fluctuations in aerosol-related properties. Therefore, in the inertial subregion, the extinction coefficient power spectral density is

$$S_{\beta_{\text{ext}}}(f) = (2\pi/U) S_{\beta_{\text{ext}}}(\kappa) = 0.25 C_{\beta_{\text{ext}}}^2 (2\pi/U)^{-2/3} f^{-5/3}$$

$$S_{\beta_{\text{ext}}}(f) = (2\pi/U) S_{\beta_{\text{ext}}}(\kappa) = 0.25 C_{\beta_{\text{ext}}}^2 (2\pi/U)^{-2/3} f^{-5/3} \quad (11)$$

The extinction coefficient structure parameter  $C_{\beta_{\text{ext}}}^2$  can be converted to the imaginary part of the AERISP according to equation (4). The coefficient in Eq. (11) is 0.25 (Wyngaard et al., 1971). It has been suggested in the literature that the coefficient for the spectral density should be 0.125 (Gibbs and Fedorovich, 2020). The difference between the two coefficients 0.25 and 0.125 is whether the integral of the spectral density is equal to the variance or half of the variance. If the integral of the spectral density is equal to the variance, the coefficient of 0.25 is taken; if the integral of the spectral density is equal to half of the variance, the coefficient is taken as 0.125. According to the spectral density curve, the coefficients are determined within the inertial subregion, and the structure parameters  $C_{\beta_{\text{ext}}}^2$  can be obtained. According to the relationship between the extinction coefficient and the imaginary part of the AERI in Eq. (4), the imaginary part of the AERISP can be obtained as  $C_{n, \text{Im}}^2$ .

302 Similarly, power spectral density profiles with temperature fluctuations that

$$303 \quad S_T(f) = (2\pi/U)S_T(\kappa) = 0.25C_T^2(2\pi/U)^{-2/3}f^{-5/3}$$

$$304 \quad S_T(f) = (2\pi/U)S_T(\kappa) = 0.25C_T^2(2\pi/U)^{-2/3}f^{-5/3} \quad (12)$$

305 The actual temperature turbulence spectral density profile often takes the form of a von Karman  
306 spectrum as

$$307 \quad S_T(f) = 0.25C_T^2(2\pi/U)^{-2/3} \left( f^2 + \left( \frac{U}{2\pi L_0} \right)^2 \right)^{-5/6}$$

$$308 \quad S_T(f) = 0.25C_T^2(2\pi/U)^{-2/3} \left( f^2 + \left( \frac{U}{2\pi L_0} \right)^2 \right)^{-5/6} \quad (12')$$

309 Based on the relationship between the temperature and the real part of the AERI, we have

$$310 \quad C_n^2 = C_T^2 / R_{TN}^2 C_{n,Re}^2 = C_T^2 / R_{TN}^2 \quad (13)$$

311 where  $R_{TN}$  denotes the coefficient of proportionality between the change in the real part of the AERI  
312 and the change in atmospheric temperature.

$$313 \quad R_{TN} = \frac{dT}{dn_{Re}} = 1.29 \times 10^4 \times \left( 1 + \frac{7.52 \times 10^{-3}}{\lambda^2} \right)^{-1} \frac{\bar{T}^2}{P}$$

314 where  $R_{TN}$  denotes the coefficient of  
315 proportionality between the change in the real part of the AERI and the change in atmospheric  
temperature (Tatarskii, 1961; Zhou et al., 1991).

$$316 \quad R_{TN} = \frac{dT}{dn_{Re}} = -1.29 \times 10^4 \times \left( 1 + \frac{7.52 \times 10^{-3}}{\lambda^2} \right)^{-1} \frac{\bar{T}^2}{P} \quad (14)$$

317 where the wavelength  $\lambda$  is in microns, the atmospheric pressure P is in hectopascals, and the  
318 temperature T is in kelvin.

319 The real part of the AERISP can be obtained by fitting the experimental data using Eqs. (12) or  
320 (12').

## 321 2.3 Flux estimation

322 The method for estimating the AERISP was given in the former sections. The purpose of  
323 estimating the AERISP in this paper is to estimate the aerosol flux in the near-surface layer. Here,  
324 the method of estimating the aerosol flux based on the AERISP will be given first, and then the  
325 method of estimating the aerosol vertical transport flux based on the EC technique will be  
326 introduced.

### 327 2.3.1 Optical transmission Light propagation method

328 Experiments have shown that the AERISPs satisfy the theory of surface layer similarity; thus,  
329 (Yuan et al., 2019)

$$F_{a\_LAS} = \left( \frac{C_{n,lm}^2}{C_{n,Re}^2} \right)^{1/2} \frac{R_{MN}}{R_{TN}} u_* |T_*| \quad F_{a\_LAS} = \left( \frac{C_{n,lm}^2}{C_{n,Re}^2} \right)^{1/2} \frac{R_{MN}}{R_{TN}} u_* |T_*| \quad (15)$$

where  $u_*$  is the friction velocity and  $T_*$  is the characteristic potential temperature. These two parameters can be determined from the wind speed and temperature profiles. The real and imaginary parts of the AERISP are determined from LAS measurements. The  $R_{MN}$  can be obtained from aerosol mass concentration and visibility measurements ( $R_{MN} = M/n_{lm}$ , where  $M$  is the aerosol mass concentration approximated as  $PM_{10}$  and  $n_{lm}$  can be determined from visibility measurements) (Yuan et al., 2021), and the  $R_{TN}$  can be calculated from the mean air temperature and other measurements using Eq. (14) again.

When turbulence in the surface layer is developed, Eq. (15) can be approximated as (Yuan et al., 2019),

$$F_{a\_LAS} = a \left( \frac{g}{T} \right)^{1/2} R_{TN}^{1/2} (C_{n,Re}^2)^{1/4} R_{MN} (C_{n,lm}^2)^{1/2} (z-d)$$

$$F_{a\_LAS} = a \left( \frac{g}{T} \right)^{1/2} R_{TN}^{1/2} (C_{n,Re}^2)^{1/4} R_{MN} (C_{n,lm}^2)^{1/2} (z-d) \quad (16)$$

Here,  $a$  is the scale factor with a theoretical value of 0.567 (which needs to be determined by comparative experiments),  $g$  is the gravitational acceleration,  $z$  is the scintillator height, and  $d$  is the zero-plane displacement. Equation (16) does not require measurements of the  $u_*$  and  $T_*$  data. Generally, the measurement heights are high, and the assumption of developed turbulence in the surface layer is easily met during the day under unstable conditions.

### 2.3.2 Based on single-point eddy covariance

Eddy covariance is a commonly used method for the measurement of Earth air exchange fluxes in the near-surface layer. Using rapid measurements of the vertical wind speed and extinction coefficient to obtain the ups and downs of the vertical wind speed and extinction coefficient, the expression for the vertically transported aerosol flux calculated by the eddy-covariance method with the mean vertical velocity close to zero is given by (Wilczak et al., 2001)

$$F_{a\_EC} = R_{MN} \frac{\lambda}{4\pi} \overline{w' \beta'_{ext}} \quad F_{a\_EC} = R_{MN} \frac{\lambda}{4\pi} \overline{w' \beta'_{ext}} \quad (17)$$

The prime' in Eq. (17) denotes fluctuation.

## 2.4 Introduction to the experiment

The experiments were performed on the campus of the University of Science and Technology of China (USTC) in Hefei, Anhui Province, China. The campus of the University of Science and Technology of China (USTC) is located in downtown Hefei. Figure 1a gives part of the Hefei city area, where the red rectangle corresponds to Fig. 1b, the campus of the USTC. The campus is surrounded by four highways, and the two highways in the west and north have more vehicles, especially the viaducts in the west. The campus is composed of vegetation, roads and teaching buildings. As can be seen in Fig. 1b, green vegetation covers most of the campus. The roofs of the school buildings are almost on a plane with the tree canopy and are approximately 17 meters above the ground. The zero plane displacement in Eq. (16) is taken 17 meters. ( $z_H = 17$  m).

带格式的： 字体： 倾斜

带格式的： 段落间距段前： 0 磅， 段后： 3.9 磅

365 Thus, the zero-plane displacement was 11.4 m ( $17 \times 0.67=11.4$ ) (Shao et al., 2021; Grimmond and  
366 Oke, 1999; Leclerc and Foken, 2014). There are two tall buildings (T and R in Fig. 1b) at the  
367 southernmost and northernmost parts of the campus, and the distance between the two buildings is  
368 approximately 960 meters. The experiment consists of two parts: one part ~~is to carry~~ consists of  
369 carrying out the light propagation experiment using a self-developed large aperture scintillator  
370 (LAS), and the other part ~~is to carry~~ consists of carrying out the measurement using the instruments  
371 on the meteorological tower in the middle of the beam. ~~(the details of the instruments are listed in~~  
372 ~~Table 1).~~ The transmitting end of the LAS was installed on the 12th floor of the southernmost  
373 building (T in Fig. 1b), the receiving end was installed on the 12th floor of the northernmost building  
374 (R in Fig. 1b), and the distance of the beam from the ground was approximately 35 meters. The  
375 apertures of the transmitting and receiving ends were 250 mm. The sampling frequency of the  
376 receiving end was 500 Hz, and a data file was saved every 30 minutes. The height of the  
377 meteorological tower is 18 meters above the roof of ~~athe~~ teaching building (P in Fig. 1b). The ~~height~~  
378 ~~of the~~ top of the meteorological tower is equal to the height of the beam. The meteorological tower  
379 is equipped with 5 layers of wind speed ~~and, wind~~ direction, temperature and humidity measurement  
380 sensors. At the top of the tower, there is a radiation quadrature sensor, and at the bottom of the tower,  
381 there is a rainfall measurement sensor. In this paper, we use data from the top 18 ~~meter meters of~~  
382 height ~~position~~ of the meteorological tower with sensors installed for conventional meteorological  
383 parameters, including temperature, humidity, wind speed, ~~and~~ wind direction ~~and~~ radiation.  
384 Conventional meteorological data ~~are were~~ collected at 1-second intervals, average data ~~are were~~  
385 obtained every half hour after data collection, and precipitation data ~~are were~~ recorded every half  
386 hour. A three-dimensional sonic anemometer thermometer was installed at the top of the tower, and  
387 ~~athe~~ high-frequency sampling visibility sensor CS120A (Campbell, 2012) was upgraded to ~~have the~~  
388 ~~ability to~~ obtain a 1-Hz visibility (Ren et al. 2020). ~~The~~ three-dimensional sonic anemometer  
389 thermometer can obtain a sampling frequency of ~~over~~ 10 Hz and is a common instrument used in  
390 atmospheric turbulence research; as such, we will not introduce it in depth. To correlate the vertical  
391 wind speed with the extinction coefficient to obtain the aerosol flux, the data collected by the sonic  
392 anemometer-thermometer at 10 Hz were averaged to obtain 1-Hz data, which were saved in a data  
393 file. ~~By doing so, the aerosol flux only contains eddies with a frequency lower than 1 Hz; in other~~  
394 ~~words, any turbulent eddy, whose frequency is higher than 1 Hz, is automatically eliminated. By~~  
395 ~~comparing the T-w correlations calculated from the 10 Hz data and the 1 Hz data, it can be seen that~~  
396 ~~the error due to this high-frequency neglect is less than 5% (details in Appendix).~~

397 The time period of the experiment is January 9-23, 2022, a total of 15 days. ~~The winter period~~  
398 ~~was chosen, because it is considered to be typical of this period, with mainly sunny days, weak~~  
399 ~~rainfall, and relatively high pollution in winter.~~

## 400 2.5 Data quality control

401 ~~Data~~ ~~The quality of the data~~ obtained from field observations ~~need~~ needs to be controlled ~~for data~~  
402 ~~quality~~ before further processing (Foken and Wichura, 1996). This study involves several types of  
403 data, mean variables, cumulative variables, and fluctuating variables. ~~Mean~~ ~~The mean~~ variables  
404 ~~include~~ ~~included~~ 30-minute averages of temperature, humidity, wind speed, wind direction, and  
405 global radiation. Data quality control for mean variables was performed by comparing measurements  
406 at different heights or different sites. The same variables with the same trend at different heights and  
407 different locations were considered ~~to be~~ high-quality data. All ~~the~~ measured mean data were  
408 determined to be satisfactory. ~~Cumulative~~ ~~The cumulative~~ variables refer to 30-minute rainfall data.

带格式的：字体颜色：黑色

带格式的：缩进：左侧：0.02 厘米，首行缩进：0.72 厘米，段落间距段前：0 磅，段后：3.9 磅，行距：多倍行距 1.23 字行

---

409 Rainfall data were qualified with reference to relative humidity, total radiation and air temperature.  
410 ~~Fluctuating~~The fluctuating data included 10-Hz ultrasonic anemometer data and 1-Hz visibility data,  
411 as well as high-frequency intensity fluctuation data measured by the LAS, the real and imaginary  
412 parts of the AERISP, and calculated aerosol fluxes. Quality control consisted mainly of eliminating  
413 spikes and replacing missing data.

414 The reason for the spike points in the light intensity fluctuation data is that the received signal  
415 jumps when there are flying birds and other obstructions to the optical signal on the propagation path.  
416 This situation is automatically determined by the program. When this occurs, the data for that time  
417 period ~~will~~are not ~~be~~ processed. The AERISP and aerosol flux data are judged according to (a) three  
418 times the standard deviation (SD) from the mean value and (b) three times the standard deviation  
419 from the mean of differences between adjacent moment data. To determine the three times ~~standard~~  
420 ~~deviation~~the SD from the mean value, the trend is obtained by averaging over a two-hour period,  
421 then calculating the difference between the measured value and the trend at each moment, calculating  
422 the mean and variance of the difference, and considering a spike point if the difference is outside ~~the~~  
423 3 times ~~standard deviation~~the SD. The 3 times ~~standard deviation~~the SD of adjacent differences is  
424 determined by first calculating the difference between adjacent moments and then calculating the  
425 mean and ~~standard deviation~~SD of the difference. Any data that deviates from the mean by more than  
426 3 times the ~~standard deviation~~SD is considered a spike point.

427 ~~Data~~The data judged to be ~~a~~spikespikes will be supplemented by the average of adjacent  
428 moments. Of course, ~~the~~ data processed according to this method appear to be completely missing  
429 for longer time periods. For such cases, no further methods to realize supplementation are considered  
430 in this paper. There are other errors in measurements made with the LAS ~~that are~~due to specific  
431 reasons (Moene et al., 2009); for example, the effect of spectral shape deviations using the von  
432 Karman model and intermittent variations in the properties of this spectrum on the LAS signal ~~is~~are  
433 not considered in this study.

434 ~~Similar to~~Like for CO<sub>2</sub> flux ~~calculation~~calculations, EC calculations for aerosol flux were  
435 performed to obtain aerosol fluxes, and several data quality control ~~work was~~studies were conducted,  
436 such as coordinate system rotations(Wilczak et al., 2001;Yuan et al., 2011), ~~and~~ WPL  
437 corrections(Webb et al., 1980).

## 438 3 Experimental results

439 In the following, the variation curves of conventional meteorological parameters during the  
440 experimental period, individual examples of AERISPs, a comparison of the two methods for the  
441 results of multiday continuous observations and a comparison of the two methods for the results of  
442 flux measurements ~~will be~~are presented to verify the reliability of the means of light propagation  
443 ~~measurement~~measurements.

### 444 3.1 General meteorological parameters and extinction 445 coefficients

446 The variation curves of conventional meteorological parameters during the experiment,  
447 including temperature, humidity, wind speed, wind direction, radiation and precipitation, and  
448 extinction coefficient are shown in Fig. 2, where the extinction coefficient is calculated from the

---

449 visibility ( $\beta_{ext} = 3.912/V$ ,  $V$  denotes visibility). Seven days during the experiment were sunny, and  
450 four of the remaining eight days had rainfall. The temperatures on sunny days were characterized by  
451 significant daily variations, with a minimum temperature of 0.4°C, and the maximum diurnal  
452 temperature difference could reach more than 9°C. ~~Relative~~The relative humidity exceeded 80% for  
453 only a few periods during ~~the~~ sunny days. The wind speed was generally less than 3 m/s, and there  
454 were ~~only~~ very few periods of north wind with a speed ~~of more~~ greater than 3 m/s. There was no  
455 obvious prevailing wind direction during the experimental period, and only the north wind was  
456 equivalent to the other directions with a slight predominance. The meteorological conditions during  
457 the experiment were similar to those of the local winter season. The extinction coefficient curve with  
458 time during the experiment is given in Fig. 2(g). The pollution gradually increased from the 9th to  
459 Jan. 13th and decreased on the 13th; from the 14th to the 20th, the pollution gradually increased and  
460 decreased on the 20th. The meteorological conditions during the experimental period can be  
461 considered typical.

## 462 3.2 Example results from measurements of the imaginary part 463 of the AERISP

464 Before carrying out the comparison of the measurement results of the two methods for obtaining  
465 the AERISP, the comparison of the measurement results of an individual example is given. The  
466 experimental data measured from 2022-01-16 13:00-13:30 will be used here as an example to  
467 illustrate the calculation of the AERISP, and the results will be given. This time period is midday on  
468 a clear day (shown in Fig. 2e), and both the total radiation and sensible heat fluxes are large, so this  
469 time period can be taken as a good typical example.

### 470 3.2.1 Structure parameters obtained by light propagation

471 The AERISP is first ~~given~~ described using the light propagation method. The sequence of light  
472 intensity signals obtained at the receiving end is shown in Fig. 3a. The time duration is 2022-01-16  
473 13:00-13:30, and the sampling frequency is 500 Hz, ~~so~~ thus there are 900000 data points in the time  
474 series of light intensity ~~fluctuation~~ fluctuations in Fig. 3a. The curve has both low- and high-  
475 frequency fluctuations. Using spectral analysis and correlation analysis, the variance ~~of~~ in the low-  
476 frequency part of the logarithmic light intensity is 1.08e-4, and the variance ~~of~~ in the high-frequency  
477 part is 5.06e-4. The solid dots in Fig. 3b are the measured spectral densities of the logarithmic light  
478 intensity fluctuations, and the black dashed lines and solid lines represent the results calculated by  
479 Eqs. (6) and (9), respectively, and represent the contributions of the imaginary part and the real part.  
480 As seen from the power spectral density curves of the logarithmic light intensity fluctuations in Fig.  
481 3b, the high-frequency part and the low-frequency part have different characteristics.

482 In the logarithmic plot, the low-frequency part is prominent with a much higher spectral density  
483 than the high-frequency part. Theoretical analysis ~~shows~~ revealed that the low-frequency part  
484 corresponds to the contribution of the imaginary part of the AERISP. The high-frequency part is flat  
485 plus high-frequency attenuation. The high-frequency part corresponds to the contribution of the real  
486 part. The part greater than 100 Hz is noise.

487 Based on the previous theoretical approach, the spectral density fitting for the low-frequency  
488 part, while constrained by the low-frequency variance, yields an equivalent refractive index structure

---

489 parameter of  $1.14 \times 10^{-25} m^{-2/3}$ . Correspondingly, the structure parameter of the real part of the  
490 refractive index, based on the high-frequency variance, is obtained as  $2.54 \times 10^{-14} m^{-2/3}$ .

### 491 **3.2.2 Obtaining the imaginary part of the AERISP based on** 492 **the spectrum**

493 The coefficients of the power spectral density curves are proportional to the refractive index  
494 structure parameters, from which they can be determined. The extinction coefficient structure  
495 parameter can be deduced from the power spectral density of the extinction coefficient fluctuation,  
496 and the temperature structure parameter can be deduced from the power spectral density of the  
497 temperature fluctuation. The [fluctuations in the](#) extinction coefficient (Fig. 4a) and temperature (Fig.  
498 4b) [fluctuation](#) with time for the period 2022-01-16 13:00-13:30 are [given shown](#) in Fig. 4. As shown  
499 in Fig. 4, the extinction coefficient curve has more noise, while the temperature curve has less noise.  
500 On the temperature fluctuation curve, there are five distinct ramp structures.

501 Power spectral analysis of the data in Fig. 4 was carried out to obtain the power spectral density  
502 in Fig. 5. From the extinction coefficient power spectral density curve in Fig. 5a, it can be seen that  
503 spectral densities greater than 0.05 Hz exhibit noise, and spectral densities less than 0.05 Hz have  
504 inertial subregions. [When practically analyzed](#) [According to practical analysis](#), the inertial subregion  
505 ranges from 0.002 Hz to the noise onset frequency. The motion of aerosol particles in the atmosphere  
506 conforms to the "-5/3" law of turbulence. The extinction coefficient structure parameter was obtained  
507 by fitting the data in the inertial subregion using Eq. (11) with a value of  $3.9 \times 10^{-11} m^{-2} m^{-2/3}$ ,  
508 which was then converted to the structure parameter of the imaginary part of the refractive index of  
509  $1.04 \times 10^{-25} m^{-2/3}$ .

510 Correspondingly, as seen from the temperature fluctuation power spectrum [density](#) curve in Fig.  
511 5b, almost no noise appears, which is mainly due to the small [amount of noise](#) [of in](#) the temperature  
512 signal itself, while the 1 Hz temperature data here are obtained by averaging the data collected at 10  
513 Hz. The temperature structure parameter of  $0.0218^\circ C^2 m^{-2/3}$  is obtained by fitting using Eq. (12),  
514 which is converted to a refractive index real part structure parameter of  $2.1 \times 10^{-14} m^{-2/3}$ .

515 The imaginary part of the AERISP obtained by using a visibility meter and the real part of the  
516 AERISP obtained by an ultrasonic anemometer are in good agreement with the previous results given  
517 by using optical propagation [methods](#).

### 518 **3.3 Comparison of all [the](#) results for the AERISP**

519 The previous section gives an individual example. A comparison of all the data during the  
520 experiment is given below, as shown in Figs 6 and 7.

521 A comparison of the time series of AERISPs measured by the two methods is given in Fig. 6,  
522 where Fig. 6a shows the time series of the imaginary part of the AERISP and Fig. 6b shows the time  
523 series of the real part of the AERISP. [It can be seen that there](#) [There](#) are large fluctuations in the  
524 imaginary part of the AERISP during the experimental period. This trend is close to that of the  
525 aerosol extinction coefficient. [From Fig-Figure 6a, it can be seen shows](#) that there is no obvious daily  
526 variation characteristic. The trend agreement of the results obtained by the two methods is very good.  
527 From Fig. 6b, it can be seen that the real part of the AERISP on sunny days has obvious daily  
528 variation characteristics, [which; these characteristics](#) are large during the day and small at night. The

agreement of the results obtained by the two methods is good during the daytime, day (8:00-17:00), and at night, the results obtained by the light propagation method are larger than those of the large point measurements.

Scatter plots of the results of the measurements of the two methods are given in Fig. 7. Figure 7a shows the scatter plot of the results of the two methods for the imaginary part of the AERISP with almost the same correlation coefficient  $R^2$  of 0.73 for daytime and nighttime, while Fig. 7b shows the scatter plot of the results of the two methods for the real part of the AERISP with a correlation coefficient of real  $R^2$  of 0.62 for daytime and 0.15 for nighttime. This shows that the correlation coefficients of the imaginary structure parameters part of the AERISP obtained by the two methods are larger than those of the real structure parameters. The reason for the smaller almost equal during both daytime and nighttime, and the correlation coefficient of the real part of the AERISP is that the difference in the real part of the AERISP obtained by the two methods is smaller at night is larger than during the daytime. This shows that the aerosol spatial distribution of aerosol at night may be more homogeneous than the temperature distribution. The reason for this difference may be that the temperature distribution in the overlying surface of the campus at night is not uniform, and weak turbulence does not produce strong mixing, resulting in a non-uniform distribution of the real part of the AERISP. There are no strong aerosol emission sources on the nighttime campus, so the distribution of the imaginary part of the AERISP behaves more uniformly.

### 3.4 Velocity-extinction coefficient correlation for a single point

To calculate aerosol fluxes using EC techniques, a delayed correlation of the vertical velocity and extinction coefficient is needed. The delayed correlation curves of the vertical velocity and extinction coefficient are given in Fig. 8.

The horizontal coordinate of the delay correlation curve in Fig. 8 is the delay time  $\tau$ , and the vertical coordinate is the delay correlation. From Fig. 8, it can be seen that at  $\tau = -2$  s, the correlation curve has an obvious extreme value, which is also the minimum value of the delay time for a duration of 300 s. The minimum value is  $-5.22 \times 10^{-6} \text{ m}^{-1}$ . The reason that the extreme value of the correlation curve does not appear at 0 s is that because there is a distance of about 0.20 m between the sensing element of the visibility meter and that of the ultrasonic anemometer. Here are given, we present the cases with obvious extremes, and there are some cases where no obvious extremes appear. In such cases where there are no significant extremes, the value associated with a delay time of 0 seconds is taken.

### 3.5 Flux

The AERISP was given in the former part, and the aerosol vertical transport flux can be estimated for the duration of 2022-01-16 13:00-13:30 according to Eq. (16),

$$F_{a,LAS} = 0.567 * \left(\frac{9.8}{283}\right)^{\frac{1}{2}} * (1.01 \times 10^6)^{\frac{1}{2}} * (2.54 \times 10^{-14})^{\frac{1}{2}} * 6216 * (1.14 \times 10^{-25})^{1/2} * 18 * 10^9 = 1.60 \mu\text{g m}^{-2} \text{ s}^{-1} \quad (18)$$

Where  $g=9.8 \text{ m/s}^2$ ,  $T=283 \text{ K}$ ,  $R_{TN} = 1.01 \times 10^6 \text{ K}$ ,  $C_{n,Re}^2 = 2.54 \times 10^{-14} \text{ m}^{-2/3} \text{ s}^{-2/3}$ ,  $R_{MN} = 6216 \text{ Kg} \cdot \text{m}^{-3}$  (Yuan et al., 2015),  $C_{n,Im}^2 = 1.14 \times 10^{-25} \text{ m}^{-2/3} \text{ s}^{-2/3}$ ,  $z=35 \text{ m}$ , and  $d=17 \text{ m}$ .

Similarly, the aerosol flux is obtained from the eddy covariance method according to Eq.(17)

带格式的: 字体: 倾斜



$$F_{a,EC} = -0.522 \times 10^{-6} * 6216 * 10^9 * \frac{0.65 \times 10^{-6}}{4\pi} = -1.67 \mu\text{gm}^{-2} \text{s}^{-1} \quad (19)$$

570 ~~Where~~  $w' \beta_{ext}' = -0.522 \times 10^{-6} \text{s}^{-1} \text{s}^{-1}$ ,  $R_{MN} = 6216 \text{Kg}$  ~~6216 Kg~~  $\cdot \text{m}^{-3}$ , ~~and~~  $\lambda = 0.65 \times$   
 571  $10^{-6} \text{m}$ .

572 From the previous calculations, we can see that during the half hour ~~from~~ 2022-01-16 13:00-  
 573 13:30, the absolute values of the aerosol fluxes ~~obtained~~ by the two methods are very close, but of  
 574 opposite ~~signs~~. Since the LAS method based on light propagation cannot determine the direction  
 575 of flux transport, only the magnitude of the flux can be ~~given~~ determined. This is similar to the fact  
 576 that the estimation of surface sensible heat fluxes using ~~an~~ LAS ~~also gives~~ provides information  
 577 ~~about~~ only the magnitude but not the direction. There are some judgments for estimating the direction  
 578 of sensible heat flux using a LAS, such as those based on sunrise and sunset times and atmospheric  
 579 stability (Zhao et al., 2018). Here, ~~the flux is~~ negative ~~to indicate~~ flux indicates the deposition of  
 580 aerosol particles. Because the experimental site is a campus, there is almost no source of aerosol  
 581 particle emission in the overlying surface, which is manifested as a sink of aerosol particles inside  
 582 the city. Therefore, the direction of aerosol flux ~~measurement~~ measurements based on the LAS needs  
 583 to be judged based on the nature of the ~~subsurface~~ surface.

584 The results of aerosol flux calculations throughout the experiment, except ~~for~~ two days of rain,  
 585 the 22nd and 23rd ~~days~~. are given in Fig. 9. Figure 9a shows the absolute values of the aerosol  
 586 vertical transport fluxes measured by the two methods based on the imaginary part of the AERISP  
 587 and EC methods, and Fig. 9b shows the aerosol vertical transport fluxes with ~~signs~~ for transport  
 588 direction measured, which correspond to the ~~rectangle~~ rectangular-point line in Fig. 9a. The trend of  
 589 aerosol fluxes obtained by the two methods given in Fig. 9a is consistent with ~~the~~ diurnal variation  
 590 in aerosol fluxes on sunny days, with larger values of aerosol fluxes at noon. At night, the aerosol  
 591 flux values are ~~smaller~~. ~~Based on a comparison between Fig. 9a and Fig. 9b, it is shown~~ lower. ~~As~~  
 592 ~~shown in Fig. 9(a), the absolute value of the aerosol flux obtained by the LAS is greater than that~~  
 593 ~~obtained by the EC at noontime on 10-11 Jan, 2022. This is because the imaginary parts of the~~  
 594 ~~AERISP obtained by the LAS are larger than those obtained by the EC, as shown in Fig. 6a. Another~~  
 595 ~~possible reason is that it was a cloudy day during both the 10th and 11th days, there was a weak~~  
 596 ~~rainfall process on the 10th day at 16:00, and the winds on the 10th and 11th days were lighter and~~  
 597 ~~had a greater change in direction. The turbulence during noontime on 10-11 is weaker, resulting in~~  
 598 ~~an inhomogeneous horizontal distribution and a large difference in measurements between the two~~  
 599 ~~methods.~~

600 ~~A comparison of Fig. 9a and Fig. 9b, reveals~~ that the aerosol flux is negative at noon on clear  
 601 days, indicating that the turbulence is strong at noon, which enhances the downward transport of  
 602 aerosol particles.

603 This study was conducted ~~in~~ on a campus with no emission sources, and the downward flux  
 604 ~~is~~ was reasonable; in fact, there was an upward flux measured by the EC method if there were  
 605 emission sources in the observation area (Ren et al. 2020).

## 606 4 Conclusion and discussion

607 To validate the previously developed method of measuring the AERISP and ~~the~~ aerosol mass  
 608 flux, this paper theoretically organizes the concept of the AERISP, introduces two methods ~~off~~  
 609 measuring the AERISP and estimating the aerosol vertical transport flux by using the AERISP and  
 610 EC methods, and carries out field observation experiments in an urban area. The experimental results

---

611 show that the AERISPs estimated by the two methods are in good agreement, and the aerosol vertical  
612 transport fluxes obtained by the two methods based on the AERISP and EC are in good agreement.

613 According to the experimental results, the imaginary part of the AERISP expresses the intensity  
614 of the fluctuation  $\sigma_{\text{fin}}$  the attenuation of light during transmission. When the air-transparent band is  
615 used, the imaginary part of the AERISP characterizes the intensity of the fluctuation  $\sigma_{\text{fin}}$  the  
616 extinction coefficient of the aerosol.

617 The aerosol flux is related to both the fluctuations in aerosol concentration and the intensity of  
618 atmospheric turbulence. When there is an aerosol emission source on the overlying surface, the  
619 aerosol flux is positive, transporting aerosol particles upwards. When there is no aerosol emission  
620 source in the overlying surface, the overall performance is aerosol particle deposition and  
621 downwards flux transport ~~of flux~~. In general, urban green lands are areas of aerosol particle  
622 deposition, while ocean and desert surfaces can often be viewed as source areas for aerosols. [The  
623 large difference in the real part of the AERISP measured by the two methods at night also contributes  
624 to the large difference in the aerosol fluxes obtained by the two methods at night.](#)

625 From the experimental results, we can also see that, as a comparison, this paper also gives  
626 results for the temperature refractive index structure parameters, and as [seenshown](#) in Fig. 6, the  
627 trends for the structure parameters in the real and imaginary parts of the AERISP are different,  
628 indicating that temperature fluctuations and aerosol concentration fluctuations are uncorrelated. The  
629 purpose of this paper is to illustrate the physical significance of the ~~structure constants of the~~  
630 imaginary part of the AERISP obtained using the LAS technique and to obtain the aerosol vertical  
631 transport flux based on the AERISPs. ~~In~~When inverting the imaginary part of the AERISP using the  
632 light propagation principle, ~~thereit~~ is ~~an assumption~~[assumed](#) that the aerosol concentration  
633 fluctuations are not correlated with the temperature fluctuations. This assumption cannot be  
634 ~~proved~~[proven](#) theoretically. From the experimental results, as ~~can be seen~~[shown](#) in Fig. 6, the trends  
635 of the real and imaginary parts of the AERISP are different, indicating that the temperature  
636 fluctuations and the aerosol concentration fluctuations are uncorrelated. This phenomenon shows  
637 that the two sources are different, ~~which is and are~~ basically consistent with the actual situation. This  
638 also shows that the assumptions of the theory for obtaining the imaginary part of the AERISP are  
639 reasonable.

640 ~~In order to~~To compare with aerosol transport fluxes obtained based on the AERISPs, this paper  
641 uses ~~delayed a~~[delay](#) correlation between the visibility meter and vertical wind speed to obtain aerosol  
642 vertical transport fluxes. Currently, a modified visibility meter is utilized to obtain 1 Hz visibility  
643 data, ~~and thereafter which~~ the extinction coefficient is obtained. ~~From the~~[The](#) extinction coefficient  
644 power spectrum in Fig. 5a, ~~it can be seen~~ [shows](#) that there is a large amount of noise in the high-  
645 frequency part. The signal-to-noise ratio of the extinction coefficient data is too low compared to the  
646 temperature fluctuation or velocity fluctuation, which introduces a large error in the calculation of  
647 the aerosol flux. Although the overall trend magnitude agreement of the fluxes obtained by the two  
648 methods is good enough to show that the two methods can be corroborated with each other, there  
649 are still differences in the details, ~~which require; however,~~ technical methods [are required](#) to improve  
650 the performance of the instrument and to obtain high-quality aerosol extinction coefficient data ~~in  
651 order to~~ carry out ~~the~~ measurements of vertical aerosol transport fluxes based on [the](#) EC method at  
652 a single point.

653 **Data availability.** Requests for data that support the findings of this study can be sent to  
654 rmyuan@ustc.edu.cn.

655 **Competing interests.** The authors declare that they have no conflict of interest.  
656 **Author contributions.** Renmin Yuan and Hongsheng Zhang designed experiments and wrote the  
657 manuscript; Renmin Yuan, Jiajia Hua, Hao Liu, Xingyu Zhu and Peizhe Wu carried out  
658 experiments; Renmin Yuan analyzed experimental results. Jianning Sun revised the manuscript and  
659 participated in the discussion.  
660 **Acknowledgements.** This study was supported by the National Natural Science Foundation of China  
661 (42075131, [42105076](#)) and the National Key Research and Development Program under grant no.  
662 2022YFC3700701.

## 663 Appendix: Comparison of fluxes between 10 664 Hz and 1 Hz

665 To determine the high frequency loss due to the use of 1 Hz data for flux calculations, the T-w  
666 covariance was used to perform an analytical comparison between the fluxes obtained by sampling  
667 the data at 10 Hz and the fluxes obtained by gaining the data at a frequency of 1 Hz. The data from  
668 January 9 and 23, 2022 were processed, and the fluxes corresponding to different sampling  
669 frequencies were compared and are shown in Fig.10. There are two ways to obtain 1 Hz data: one is  
670 directly obtained at 1 Hz sampling frequency (shown in Fig. 10a), and the other is 1 Hz data obtained  
671 by averaging 10 Hz data over 10 data points (shown in Fig. 10b). In comparison, the flux calculated  
672 from the 1 Hz data obtained by averaging 10 data points is smaller (slope of 0.97). This indicates a  
673 slower response of the instrument. This is the case for the visibility meter, for which a slower  
674 response was used in this study. Based on the linear fit results and the root mean square error (RMSE)  
675 in Fig. 10, the difference in the fluxes between 10 Hz and 1 Hz is less than 5%.

676 Overall, the error due to the lower sampling frequency of 1 Hz is much smaller than the  
677 difference between the two methods discussed in this study.

678 带格式的: 缩进: 左侧: 0 厘米, 悬挂缩进: 2 字符

## 679 Reference

- 680 [1] Andrews, L. C., and Phillips, R. L.: Laser beam propagation through random media, SPIE, SPIE, Bellingham,  
681 Washington, USA, 2005.
- 682 [2] Campbell, S. L.: CS120 Visibility Sensor User Guide, Campbell Scientific Ltd., Logan, Utah 60 pp., 2012.
- 683 [3] Charlson, R. J.: Atmospheric visibility related to aerosol mass concentration - a review, *Environmental Science &*  
684 *Technology*, 3, 913-918, [10.1021/es60033a002](#), 1969.
- 685 [4] Clifford, S. F.: Temporal-frequency spectra for a spherical wave propagating through atmospheric turbulence,  
686 *J. Opt. Soc. Am.*, 61, 1285-1292, 1971.
- 687 [5] Foken, T., and Wichura, B.: Tools for quality assessment of surface-based flux measurements, *Agricultural and*  
688 *Forest Meteorology*, 78, 83-105, [10.1016/0168-1923\(95\)02248-1](#), 1996.
- 689 [6] Gibbs, J. A., and Fedorovich, E.: On the Evaluation of the Proportionality Coefficient between the Turbulence  
690 Temperature Spectrum and Structure Parameter, *Journal of the Atmospheric Sciences*, 77, 2761-2763,  
691 [10.1175/jas-d-19-0344.1](#), 2020.
- 692 [7] Gordon, M., Staebler, R. M., Liggio, J., Vlasenko, A., Li, S.-M., and Hayden, K.: Aerosol flux measurements  
693 above a mixed forest at Borden, Ontario *Atmos. Chem. Phys.*, 11, 6773-6786, 2011.
- 694 [8] Grimmond, C. S. B., and Oke, T. R.: *Aerodynamic Properties of Urban Areas Derived from Analysis of*  
695 *Surface Form*, *Journal of Applied meteorology*, 38, 1262-1292, 1999.
- 696 [9] Kaimal, J. C., Izumi, Y., Wyngaard, J. C., and Cote, R.: Spectral characteristics of surface-layer turbulence, *Q. J.*  
697 *Roy. Meteor. Soc.*, 98, 563-589, 1972.

680 带格式的: 字体: 小五

682 带格式的: 缩进: 左侧: 0 厘米, 悬挂缩进: 2 字符, 首行缩进: -2 字符, 无项目符号或编号

685 带格式的: 缩进: 左侧: 0 厘米, 悬挂缩进: 2 字符, 首行缩进: -2 字符, 无项目符号或编号

698 [7] Krieger, U. K., Marcolli, C., and Reid, J. P.: Exploring the complexity of aerosol particle properties and  
699 processes using single particle techniques, *Chemical Society Reviews*, 41, 6631-6662, 10.1039/c2cs35082c,  
700 2012.

701 [Leclerc, M. Y., and Foken, T.: \*Footprints in Micrometeorology and Ecology\*, Springer, Heidelberg, 254 pp., 2014.](#)

702 [8] Liou, K. N.: *An Introduction to Atmospheric Radiation*, 2nd Edition ed., Academic Press, California 92101-  
703 4495, USA, 2002.

704 [9] Liu, H., Yuan, R., Mei, J., Sun, J., Liu, Q., and Wang, Y.: Scale properties of anisotropic and isotropic  
705 turbulence in the urban surface layer, *Boundary-Layer Meteorology*, 165, 277-294, 2017.

706 [Martensson, E. M., Nilsson, E. D., Buzorius, G., and Johansson, C.: \*Eddy covariance measurements and\*  
707 \*parameterisation of traffic related particle emissions in an urban environment\*, \*Atmos. Chem. Phys.\*, 6, 769-  
708 785, 2006.](#)

709 [10] McNeill, V. F.: Atmospheric Aerosols: Clouds, Chemistry, and Climate, in: *Annual Review of Chemical and*  
710 *Biomolecular Engineering*, Vol 8, edited by: Prausnitz, J. M., *Annual Review of Chemical and Biomolecular*  
711 *Engineering*, 427-444, 2017.

712 [Middleton, W. E. K.: \*Vision through the Atmosphere\*, in: \*Encyclopedia of physics\*, edited by: Bartels, J., \*Geophysik\*  
713 \*II Geophysics II\*, University of Toronto Press, Toronto, 1054, 1957.](#)

714 [11] Moene, A. F., Beyrich, F., and Hartogensis, O. K.: Developments in scintillometry, *Bulletin of the American*  
715 *Meteorological Society*, 90, 694-698, 10.1175/2008bams2672.1, 2009.

716 [12] Nieveen, J. P., Green, A. E., and Kolsiek, W.: Using a large-aperture scintillometer to measure absorption and  
717 refractive index fluctuations, *Bound-Lay. Meteorol.*, 87, 101-116, 1998.

718 [13] Ren, Y., Zhang, H., Wei, W., Cai, X., and Song, Y.: Determining the fluctuation of PM2.5 mass concentration  
719 and its applicability to Monin-Obukhov similarity, *Science of the Total Environment*, 710,  
720 10.1016/j.scitotenv.2019.136398, 2020.

721 [14] Ripamonti, G., Jarvi, L., Molgaard, B., Hussein, T., Nordbo, A., and Hameri, K.: The effect of local sources on  
722 aerosol particle number size distribution, concentrations and fluxes in Helsinki, Finland, *Tellus B.*, 65,  
723 10.3402/tellusb.v65i0.19786, 2013.

724 [15] Rosenfeld, D., Andreae, M. O., Asmi, A., Chin, M., de Leeuw, G., Donovan, D. P., Kahn, R., Kinne, S.,  
725 Kivekas, N., Kulmala, M., Lau, W., Schmidt, K. S., Suni, T., Wagner, T., Wild, M., and Quaas, J.: Global  
726 observations of aerosol-cloud-precipitation-climate interactions, *Reviews of Geophysics*, 52, 750-808,  
727 10.1002/2013rg000441, 2014.

728 [Shao, B., Yuan, R., Liu, H., Qiao, B., Wang, Z., Xu, C., and Liu, G.: \*Research on Turbulence Characteristics in\*  
729 \*Urban Rough Sublayer-Taking a Site in Hefei as an Example\*, \*Journal of atmospheric and environmental\*  
730 \*optics\*, 16, 307, 2021.](#)

731 [Tatarskii, V. I.: \*Wave Propagation in a Turbulent Medium\*, McGraw-Hill Book Company Inc., New York, 1961.](#)

732 [16] van de Hulst, H. C.: *Light Scattering by Small Particles*, John Wiley & Sons, Inc., New York, 1957.

733 Vogt, M., Nilsson, E. D., Ahlm, L., Martensson, E. M., and Johansson, C.: [Seasonal and diurnal cycles of 0.25-2.5](#)  
734 [µm aerosol fluxes over urban Stockholm, Sweden](#), *Tellus B.*, 63, 935-951, 10.1111/j.1600-  
735 0889.2011.00551.x, 2011a.

736 [17] Vogt, M., Nilsson, E. D., Ahlm, L., Martensson, E. M., and Johansson, C.: Seasonal and diurnal cycles of  
737 0.25-2.5 µm aerosol fluxes over urban Stockholm, Sweden, *Tellus B.*, 63, 935-951, 10.1111/j.1600-  
738 0889.2011.00551.x, 2011b.

739 [18] Wang, T. I., Ochs, G. R., and Clifford, S. F.: Saturation-resistant optical scintillometer to measure Cn2, *J. Opt.*  
740 *Soc. Am.*, 68, 334-338, 1978.

741 [19] Webb, E. K., Pearman, G. I., and Leuning, R.: Correction of flux measurements for density effects due to heat  
742 and water-vapor transfer, *Quarterly Journal of the Royal Meteorological Society*, 106, 85-100,  
743 10.1002/qj.49710644707, 1980.

744 [20] Wilczak, J. M., Oncley, S. P., and Stage, S. A.: Sonic anemometer tilt correction algorithms, *Boundary-Layer*  
745 *Meteorology*, 99, 127-150, 10.1023/a:1018966204465, 2001.

746 [21] Wyngaard, J. C., Izumi, Y., and Collins, S. A.: Behavior of refractive-index-structure parameter near ground,  
747 *Journal of the Optical Society of America*, 61, 1646-&, 10.1364/josa.61.001646, 1971.

748 [22] Yuan, R., Luo, T., Sun, J., Zeng, Z., Ge, C., and Fu, Y.: A new method for measuring the imaginary part of the  
749 atmospheric refractive index structure parameter in the urban surface layer, *Atmospheric Chemistry and*  
750 *Physics*, 15, 2521-2531, 10.5194/acp-15-2521-2015, 2015.

751 [23] Yuan, R., Luo, T., Sun, J., Liu, H., Fu, Y., and Wang, Z.: A new method for estimating aerosol mass flux in the  
752 urban surface layer by using LAS, [Atmos. Meas. Tech. Discuss., technology, Atmospheric Measurement](#)  
753 [Techniques](#), doi:10.5194/amt-2015-301, 2016.

754 [24] Yuan, R., Zhang, X., Liu, H., Gui, Y., Shao, B., Tao, X., Wang, Y., Zhong, J., Li, Y., and Gao, Z.: Aerosol  
755 vertical mass flux measurements during heavy aerosol pollution episodes at a rural site and an urban site in the  
756 Beijing area of the North China Plain, *Atmospheric Chemistry and Physics*, 19, 12857-12874, 10.5194/acp-19-  
757 12857-2019, 2019.

758 [25] Yuan, R., Shi, C., Liu, H., Wang, Y., Qiao, B., and Wang, Z.: A method for estimating the ratio of aerosol mass  
759 concentration to the imaginary part of the atmospheric complex refractive index and its application,  
760 *Atmospheric Research*, 264, 10.1016/j.atmosres.2021.105848, 2021.

带格式的: 缩进: 左侧: 0 厘米, 悬挂缩进: 2 字符,  
首行缩进: -2 字符, 无项目符号或编号

带格式的: 缩进: 左侧: 0 厘米, 悬挂缩进: 2 字符,  
首行缩进: -2 字符, 无项目符号或编号

带格式的: 缩进: 左侧: 0 厘米, 悬挂缩进: 2 字符,  
首行缩进: -2 字符, 无项目符号或编号

带格式的: 缩进: 左侧: 0 厘米, 悬挂缩进: 2 字符,  
首行缩进: -2 字符, 无项目符号或编号

带格式的: 缩进: 左侧: 0 厘米, 悬挂缩进: 2 字符,  
首行缩进: -2 字符, 无项目符号或编号

带格式的: 缩进: 左侧: 0 厘米, 悬挂缩进: 2 字符,  
首行缩进: -2 字符, 无项目符号或编号

---

761 [26] Yuan, R. M., Kang, M., Park, S. B., Hong, J., Lee, D., and Kim, J.: Expansion of the planar-fit method to  
762 estimate flux over complex terrain, *Meteorology and Atmospheric Physics*, 110, 123-133, 10.1007/s00703-  
763 010-0113-9, 2011.

764 [27] Zhang, H., and Zhang, H.: Comparison of Turbulent Sensible Heat Flux Determined by Large-  
765 aperture Scintillometer and Eddy Covariance over Urban and Suburban Areas, *Boundary-Layer*  
766 *Meteorology*, 154, 119-136, 10.1007/s10546-014-9965-8, 2015.

767 [28] Zhao, J., Olivas, P. C., Kunwor, S., Malone, S. L., Staudhammer, C. L., Starr, G., and Oberbauer, S. F.:  
768 Comparison of sensible heat flux measured by large aperture scintillometer and eddy covariance in a  
769 seasonally-inundated wetland, *Agricultural and Forest Meteorology*, 259, 345-354,  
770 10.1016/j.agrformet.2018.05.026, 2018.

771 [Zhou, X., Tao, S., and Yao, K.: \*Advanced atmospheric physics\*, Meteorological Publishing House, Beijing, 1991.](#)

772  
773  
774

带格式的: 缩进: 左侧: 0 厘米, 悬挂缩进: 2 字符,  
首行缩进: -2 字符, 段落间距段后: 0 磅, 无项目符  
号或编号

---

775  
776

777

Table 1 details of all the instruments

<u>Meteorological elements</u>	<u>Manufacturer type</u>	<u>Sampling frequency (Hz)</u>	<u>Height (m) Above building top</u>
<u>LAS</u>	<u>Self-developed</u>	<u>500</u>	<u>18.0</u>
<u>3-D sonic anemometer</u>	<u>Campbell CSAT3</u>	<u>10</u>	<u>18.0</u>
<u>Visibility</u>	<u>Campbell CS120</u>	<u>1</u>	<u>18.0</u>
<u>Wind speed and direction</u>	<u>03001 R.M. Young</u>	<u>1</u>	<u>2.0, 4.5, 8.0, 12.0, 18.0</u>
<u>Temperature and humidity</u>	<u>Vaisala HMP155A</u>	<u>1</u>	<u>2.0, 4.5, 8.0, 12.0, 18.0</u>
<u>Radiation</u>	<u>Kipp&amp;Zonen CNR4</u>	<u>1</u>	<u>16.0</u>
<u>Precipitation</u>	<u>TE525 Tipping Bucket</u>	<u>1</u>	<u>1.0</u>

778

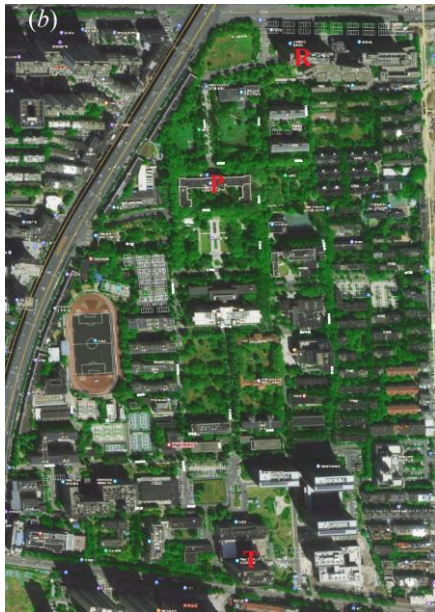
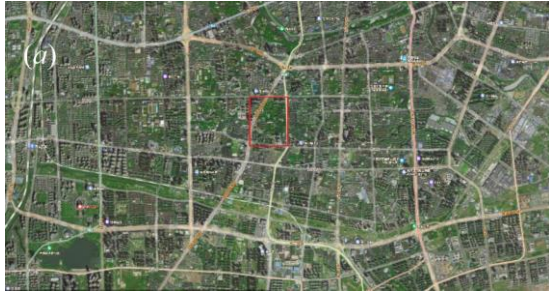
779

---

780 **Figures**

781

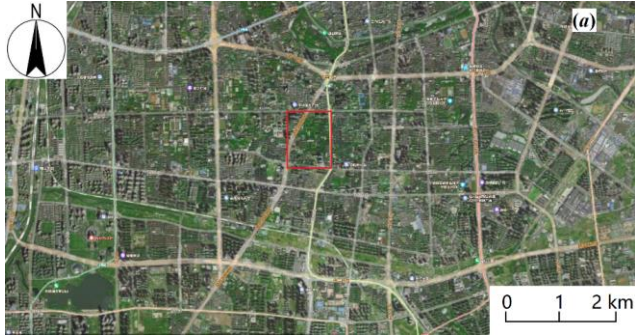
782



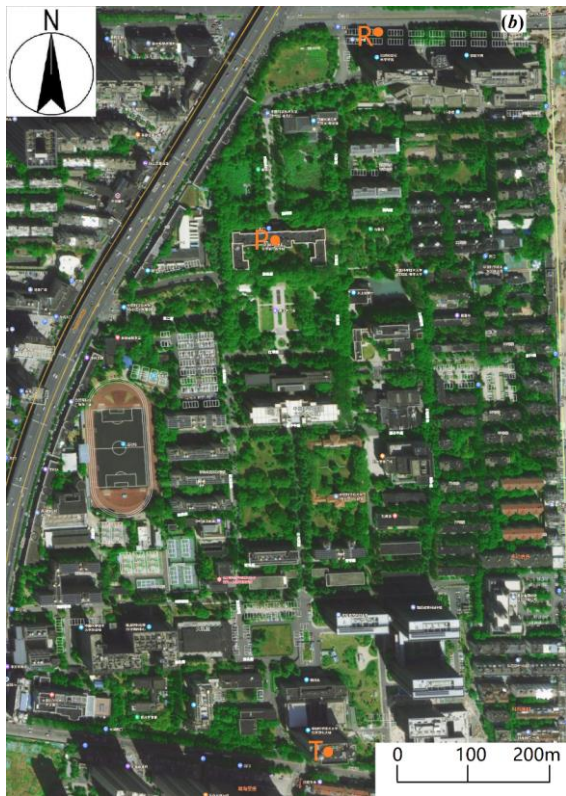
784



785



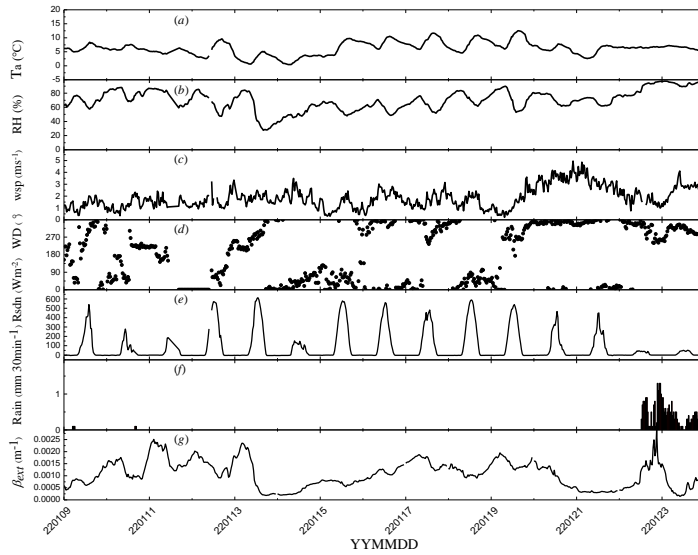
786



787

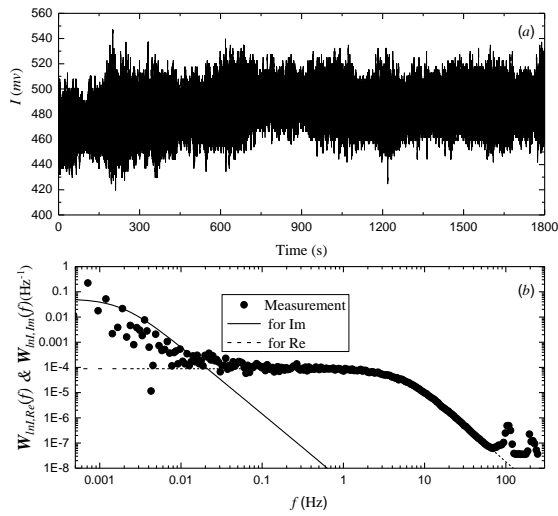
788 Figure 1. Photographs of the measurement site. (a) Map of Hefei City and (b) expanded view of  
789 the measurement site on the USTC campus, which is marked by the red rectangle in (a). Points T and  
790 R in (b) show the locations of the transmitter and receiver, respectively. Point P in (b) marks the  
791 meteorological tower position. There are four heavy traffic roads surrounding the measurement site.  
792 Figure 1a and b @ Baidu are from the following website:

793 [https://map.baidu.com/@13055953.105500832,3719556.851423825,15.3z/maptype%3DB\\_EART](https://map.baidu.com/@13055953.105500832,3719556.851423825,15.3z/maptype%3DB_EART)  
794 H\_MAP



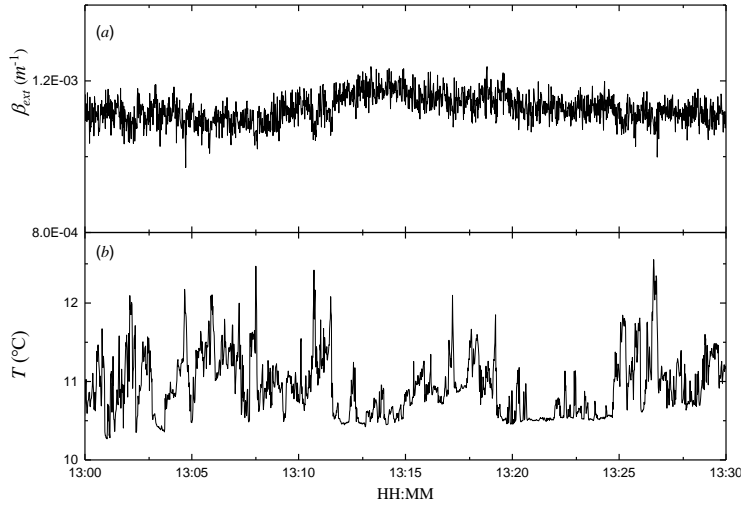
795  
796  
797  
798  
799

Figure 2. Temporal variations in the (a) air temperature (T), (b) relative humidity (RH), (c) wind speed (wsp), (d) wind direction (WD), (e) total radiation (Rsdn), (f) precipitation (Rain), and (g) extinction coefficient ( $\beta_{ext}$ ). [Details](#)The details can be found in the text.



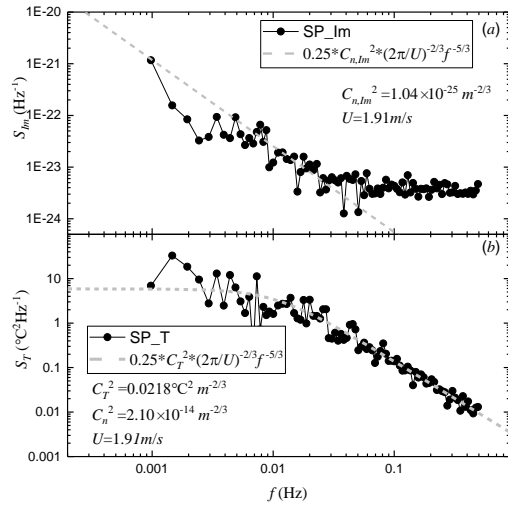
800  
801  
802

Figure 3 Temporal variations in the light intensity received by the LAS and (b) power spectral density of [the logarithm of the](#) light intensity during 2022-01-16 13:00-13:30.



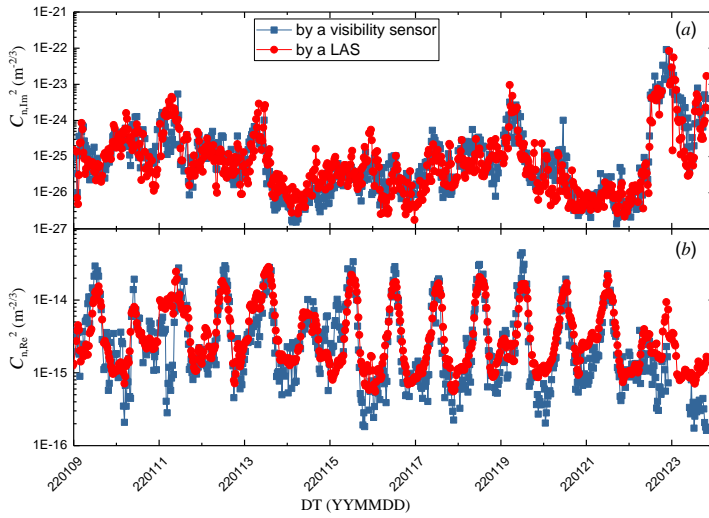
803  
804  
805  
806

Figure 4 Temporal variations in [the](#) (a) extinction coefficient and (b) air temperature during 2022-01-16 13:00-13:30.

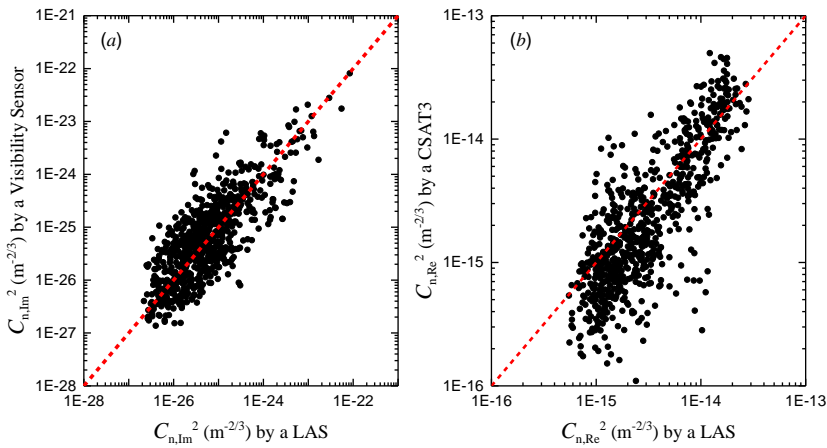


807  
808  
809

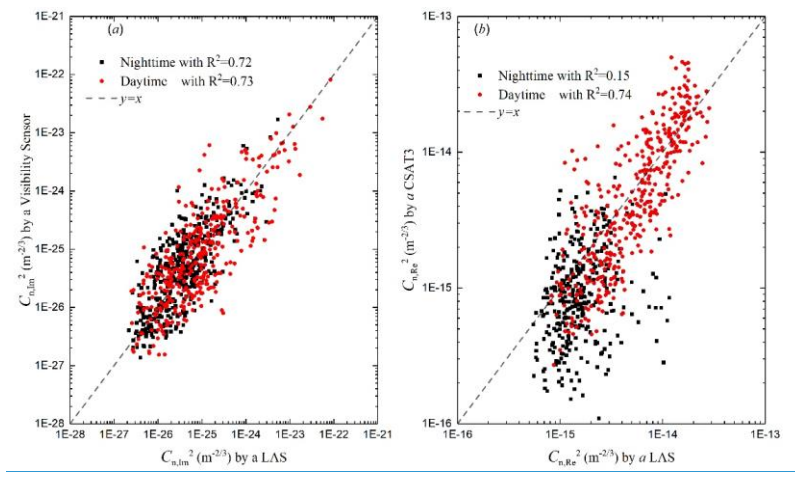
Figure 5. Power spectral density of [the](#) (a) extinction coefficient and (b) air temperature during 2022-01-16 [at](#) 13:00-13:30.



810  
 811 Figure 6. Temporal variations in (a) the imaginary part and (b) real part of the AERISP during 09-  
 812 23 Jan. 2022.



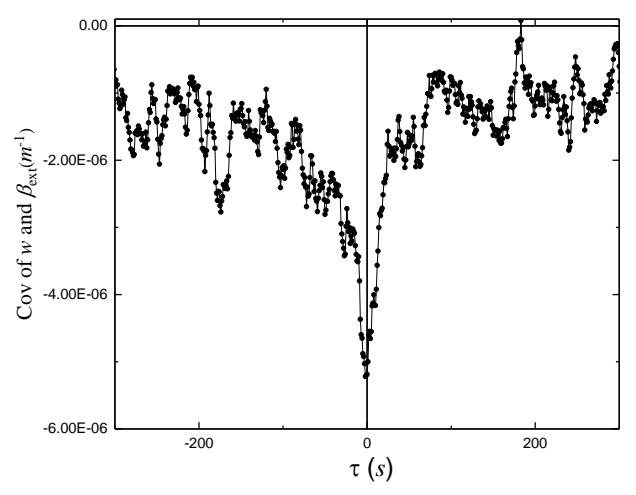
813



814  
815  
816  
817

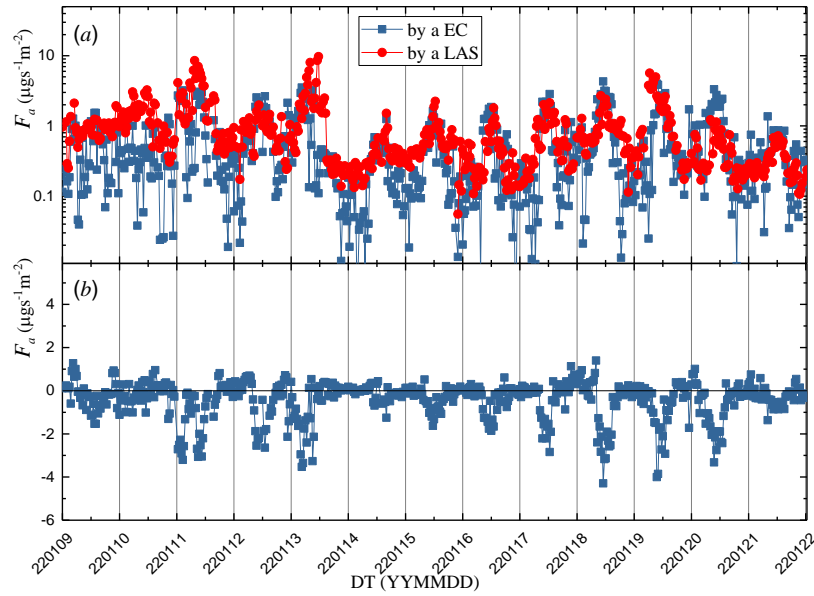
Figure 7. Comparison of (a) the imaginary part and (b) real part of the AERISP during 09-23 Jan. 2022.  
The red solid circles indicate daytime and the black solid rectangles indicate nighttime.

带格式的: 字体: 小五  
带格式的: 字体: 小五



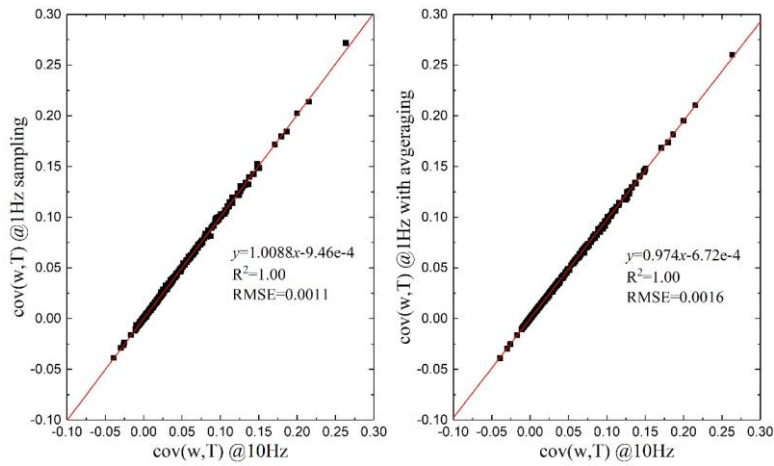
818  
819  
820

Figure 8. Delay covariance between the extinction coefficient and vertical velocity during 2022-01-16 13:00-13:30.



821  
 822 Figure 9. Temporal variations in (a) absolute value of aerosol flux based on the AERISP and EC  
 823 methods and (b) the imaginary part and (b) aerosol flux based on the EC methods during 09-21 Jan. 2022.

824  
 825



827 Figure 10 Comparison of covariance of w and T between 10 Hz and 1 Hz. with a 1 Hz sampling rate  
 828 (a) and 1 Hz data obtained by averaging 10 Hz data over 10 data points (b)

829